Ground-Based Remote Sensing of Aerosol, Clouds, Dynamics, and Precipitation in Antarctica: First Results from the 1-Year COALA Campaign at Neumayer Station III in 2023

Martin Radenz,[a] Ronny Engelmann,[a] Silvia Henning,[a] Holger Schmithüsen,[b]
Holger Baars,[a] Markus M. Frey,[c] Rolf Weller,[b] Johannes Bühl,[a] Cristofer Jimenez,[a]
Johanna Roschke,[a] Lukas Ole Muser,[b] Nellie Wullenweber,[b] Sebastian Zeppenfeld,[a]
Hannes Griesche,[a] Ulla Wandinger,[a] and Patric Seifert[a]

ABSTRACT: Novel observations of aerosol and clouds by means of ground-based remote sensing have been performed in Antarctica over the Ekström Ice Shelf on the coast of Dronning Maud Land at Neumayer Station III (70.67°S, 8.27°W) from January to December 2023. The deployment of the OCEANET-Atmosphere remote sensing observatory in the framework of the Continuous Observations of Aerosol-Cloud Interaction (COALA) campaign has brought Aerosol, Clouds and Trace Gases Research Infrastructure (ACTRIS) aerosol and cloud profiling capabilities next to meteorological and air chemistry in situ observations at the Antarctic station. We present an overview of the site, the instrumental setup, and data analysis strategy and introduce 3 scientific highlights from austral fall and winter, namely, 1) observations of a persistent mixed-phase cloud embedded in a plume of marine aerosol. Remote sensing–based retrievals of cloud-relevant aerosol properties and cloud microphysical parameters confirm that the free-tropospheric mixed-phase cloud layer formed in an aerosol-limited environment. 2) Two extraordinary warm air intrusions: one with intense snowfall produced the equivalent of 10% of the yearly snow accumulation and a second one with record-breaking maximum temperatures and heavy icing due to supercooled drizzle. 3) Omnipresent aerosol layers in the stratosphere. Our profiling capabilities could show that 50% of the 500-nm aerosol optical depth of 0.06 was caused by stratospheric aerosol, while the troposphere was usually pristine. As demonstrated by these highlights, the 1-yr COALA observations will serve as a reference dataset for the vertical structure of aerosol and clouds above the region, enabling future observational and modeling studies to advance understanding of atmospheric processes in Antarctica.

AFFILIATION: [a] Leibniz Institute for Tropospheric Research, Leipzig, Germany; [b] Alfred Wegener Institute, Helmholtz Centre for Polar and Marine Research, Bremerhaven, Germany; [c] British Antarctic Survey, Cambridge, United Kingdom

1. Introduction

The Antarctic continent and its surrounding Southern Ocean are key components of the global climate system. Having been considered rather stable over the last century, the climate of Antarctica was recently found to be changing during the last decades (Mayewski et al. 2009; Clem et al. 2020; Stammerjohn and Scambos 2020). As pointed out by Mayewski et al. (2009) and corroborated by ongoing studies (Bracegirdle et al. 2020), model projections suggest that the Antarctic interior will warm by more than 3 K, sea ice extent will decrease by approximately 30%, and precipitation will increase by about 25% over the twenty-first century. However, such projections are prone to large uncertainties (e.g., Trenberth and Fasullo 2010; Hyder et al. 2018). There is still considerable disagreement in the projections of the total radiative feedback in both polar regions (Block et al. 2020). Furthermore, global atmospheric circulation models fail to reproduce the correct cloud cover and radiative forcing of the Southern Ocean region (Franklin et al. 2013). This misrepresentation of clouds leads to biased estimates of surface radiation and sea surface temperature, which are a prerequisite for estimating the radiation and water fluxes between the ocean and the atmosphere (Lubin et al. 2020).

In general, clouds over Antarctica are common and relevant to the radiation and precipitation budgets (Adhikari et al. 2012; Bromwich et al. 2012; Listowski et al. 2019). Their characteristics, however, were not fully described so far. In particular, the frequently reported high fraction of supercooled liquid water down to temperature of the homogeneous freezing level is a subject of ongoing research (Franklin et al. 2013; Silber et al. 2019; Vignon et al. 2021). Besides the undoubted relevance, moisture, clouds, and aerosols are inseparably coupled, linked via complex pathways of interaction whose outcome manifests in the macroscopic properties of precipitation and radiation fields. On the one hand, aerosol particles are required as cloud condensation nuclei (CCN) from which cloud droplets form. On the other hand, primary ice formation in the heterogeneous freezing range from 0 to approximately −40°C requires ice nucleating particles (INP) to be present in the aerosol reservoir. The ways in which aerosol and cloud particles interact, however, are controlled by the dynamics and thermodynamics of the atmospheric environment (Morrison et al. 2012). Overall, the potential role of (the lack of) aerosol in Antarctic cloud processes has been rarely assessed so far (Mallet et al. 2023). Silber et al. (2019) related the persistent presence of supercooled drizzle formed in clouds over East Antarctica to the lack of appropriate INP, and Vignon et al. (2021) showed that realistically low INP concentrations do considerably improve the simulation of supercooled liquid layers in East Antarctic cloud systems. In a climatological perspective, it appears to be likely that an increase of polynyas, open leads, and a general decrease of sea ice cover due to global warming will be accompanied by an increase of INP concentrations from marine origin (Hartmann et al. 2020). At least for the Arctic, indication of an impact of marine biogenic INP on the thermodynamic phase of boundary layer clouds has been identified already (Griesche et al. 2021). For Antarctica, such relationships are not evident yet, but earlier studies have already found indications that the sea ice–covered Weddell Sea can act as a source of both CCN and INP over the Antarctic Peninsula (Lachlan-Cope et al. 2016).

A second major source of uncertainty is the impact of meridional transport of moisture and aerosol from the Southern Hemisphere midlatitudes and subtropics. The impact of those conditions on thermodynamics, clouds, precipitation, and radiative budget over Antarctica is not yet fully characterized (Trenberth and Fasullo 2010; Gorodetskaya et al. 2020; Ghiz et al. 2021). In the Weddell Sea sector, for instance, the relatively open space between the Weddell Sea and the South Pole is considered a highway for warm and moist air masses (Stammerjohn and Scambos 2020; Clem et al. 2020; Wille et al. 2024a,b). The associated impacts of such transport regimes, in general, referred to as atmospheric rivers, on the cloud and precipitation conditions in Antarctica are still undetermined (Lubin et al. 2020). Atmospheric rivers have also been found to be responsible for strong polynya events and associated with intensive precipitation in recent history (Francis et al. 2020). There is reason to expect a similar tendency toward an increased meridional transport of air masses from Southern Hemisphere lower latitudes toward Antarctica as it is currently observed over the Arctic (Mewes and Jacobi 2019), although the orography of Antarctica might decelerate this process in the Southern Hemisphere to some extent (Salzmann 2017). Recent studies, such as that of Wille et al. (2024a) already point to the ongoing intensification of atmospheric river events and associated strong warm-air intrusions.

International initiatives are ongoing to tackle the abovementioned scientific challenges by means of joint observational and modeling efforts as they are performed, e.g., in the framework of the Year of Polar Prediction (YOPP; Bromwich et al. 2020) and the Partnerships for Investigating Clouds and the biogeochemistry of the Atmosphere in Antarctica and the Southern Ocean (PICCAASO; Mallet et al. 2023), or large field experiments like the Atmospheric Radiation Measurement (ARM) West Antarctic Radiation Experiment (AWARE; Lubin et al. 2020). So far, remote sensing studies of the Antarctic cloud–aerosol–dynamics system concentrated on regions west of the Antarctic Peninsula, such as McMurdo Station (Nicolas and Bromwich 2011; Lubin et al. 2020), Dumont d'Urville (Grazioli et al. 2017), Syowa (Hara et al. 2014), Davis (Alexander et al. 2023), or the 5-month shipborne Measurements of Aerosols, Radiation, and Clouds over the Southern Ocean (MARCUS) campaign (Mace et al. 2021), and on spaceborne investigations. Spaceborne observations mainly rely on the A-Train satellite suite of which the Cloud–Aerosol Lidar with Orthogonal Polarization (CALIOP) aboard the *Cloud–Aerosol Lidar and Infrared Pathfinder Satellite Observations* (*CALIPSO*) and Cloud Profiling Radar (CPR) aboard *CloudSat* provided vertically resolved aerosol and cloud properties (Listowski et al. 2019; Zhang et al. 2018). Satellite profiling with active sensors, however, still often misses important details regarding clouds (Griesche et al. 2024) and precipitation in the Antarctic lower troposphere (e.g., Maahn et al. 2014) which further emphasizes the need for comprehensive, complementary surface-based measurements. Spaceborne sensors, such as CALIOP, are, for instance, not suited for the low-aerosol regime of Antarctica. It has been shown by Toth et al. (2018) that the CALIOP level 2 products fail to detect about 30% of cases when the aerosol optical depth (AOD) detected by ground-based sun photometers is 0.1 or less. This lack of detection increases gradually to 50% with surface-detected AOD of 0.05 (mean AOD over Antarctica) and approaches 100% at respective AOD values of 0.01. Sophisticated ground-based lidars can overcome those difficulties and retrieve height-resolved AOD even under the cleanest conditions and separate between tropospheric (cloud relevant) and stratospheric (ozone relevant) contributions. Also, passive satellite observations such as the Moderate Resolution Imaging Spectroradiometer (MODIS) have deficiencies in retrieving cloud optical and microphysical properties of liquid water clouds at low solar zenith angles (Grosvenor and Wood 2014) and are limited to daylight conditions. Nevertheless, spaceborne studies, the recently conducted AWARE field campaign at McMurdo Station, and MARCUS across the Southern Ocean to East Antarctica, already provided key results on the uniqueness of Antarctic clouds by putting them into

context with other regions on Earth and by enabling a generalization of detailed findings from ground-based campaigns to larger areas and longer time scales, such as demonstrated by Scott et al. (2017). For example, they confirm that Antarctic midlevel clouds produce less ice than their Arctic equivalents and that associated aerosol loads are also lowest over Antarctica (Zhang et al. 2019). Radenz et al. (2021b) also highlight the necessity of incorporating atmospheric orographic waves into studies contrasting clouds at different locations.

The lack of a comprehensive, multiseason ground-based remote sensing dataset in the Atlantic sector of Antarctica motivated a consortium of Leibniz Institute for Tropospheric Research (TROPOS) and Alfred Wegener Institute (AWI) to conduct the field experiment COALA at Neumayer Station III (70.67°S, 8.27°W; in the following just "Neumayer") on the northern edge of the Ekström Ice Shelf in Dronning Maud Land from January to December 2023. COALA is designed around a 1-yr deployment of a complex suite of ground-based remote sensing instrumentation of the OCEANET-Atmosphere observatory with the aim to provide a thorough characterization of key processes of the Antarctic climate system. Specific focus lies on 1) the determination of the spatiotemporal distribution of aerosols, pinpointing their sources, and the quantification of their optical and physical properties, including their relevance for cloud processes; 2) the documentation and study of meridional transport processes of aerosol and moisture toward Antarctica; and 3) the investigation of the macro- and microphysical properties and dynamical structure of Antarctic cloud systems and their susceptibility to aerosol perturbations. Within this article, we provide an introduction to the concept and implementation of COALA and present three highlights selected along the aims stated above: a case study of aerosol–cloud interaction in a shallow mixed-phase cloud, including microphysical retrievals; insights into the precipitation formation during two significant atmospheric river events; and exceptionally high aerosol load in the stratosphere. These three examples provide unique insight into Antarctic processes documented with a unique state-of-the-art instrumentation setup and also show the potential for more in-depth studies covering the whole observational period of 1 year.

2. OCEANET-Atmosphere mobile platform

The OCEANET-Atmosphere observatory of TROPOS has been deployed approximately 400 m south of Neumayer (70.67°S, 8.27°W, 42 m MSL; Wesche et al. 2016) in the Atlantic sector of Antarctica from January to December 2023 as shown in Fig. 1. OCEANET-Atmosphere was already frequently operated aboard the research vessels *Polarstern*, *Meteor*, and *Sonne* (Kanitz et al. 2013b; Bohlmann et al. 2018; Yin et al. 2019; Griesche et al. 2021; Engelmann et al. 2021) during Atlantic transects from the Northern Hemisphere to the Southern Hemisphere (or vice versa) or in Arctic regions, e.g., during the Multidisciplinary Drifting Observatory for the Study of Arctic Climate (MOSAiC; Shupe et al. 2022). OCEANET-Atmosphere is operated as a mobile exploratory platform in the framework of the European Aerosol, Clouds and Trace Gases Research Infrastructure (ACTRIS; Laj et al. 2024). Most of the OCEANET instruments are installed in a 20-ft container which is placed on top of a platform as shown in Fig. 1b. Table 1 and the following subsections give a brief overview of the deployed instruments.

a. Lidar Polly^XT. One core instrument is a multiwavelength polarization Raman lidar Polly^XT, which provides continuous profiles of cloud and aerosol properties (Engelmann et al. 2016).

Available retrievals cover optical parameters, aerosol microphysics (Müller et al. 1999; Baars et al. 2012; Mamouri and Ansmann 2016), aerosol typing (Müller et al. 2007; Baars et al. 2017; Floutsi et al. 2023), cloud phase estimates (Kanitz et al. 2013a; Seifert et al. 2015), liquid cloud microphysics (Jimenez et al. 2020a,b), and water vapor profiles (Dai et al. 2018).
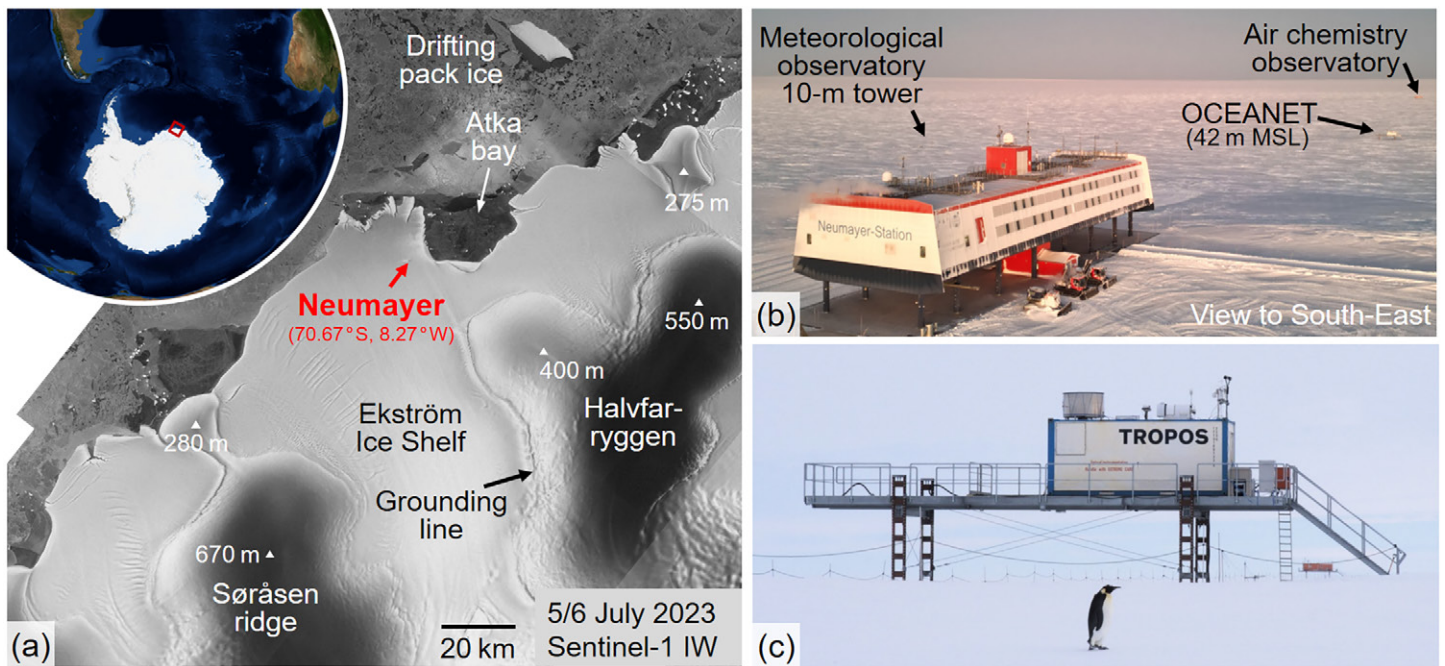
Fig. 1. Location of Neumayer Station III on the Ekström Ice Shelf. (a) Sentinel-1 synthetic aperture radar (SAR) imagery (interferometric wide swath mode) acquired on 5 and 6 Jul 2023. (b) Aerial photography depicting the surroundings of the station, including the meteorological tower, the OCEANET-Atmosphere platform, and the air chemistry observatory. (c) OCEANET-Atmosphere container as set up during the campaign.

Compared to the cloud radar (see next subsection), which operates in the microwave region, the lidar is sensitive to small scatterers, such as aerosol particles or small cloud droplets, while limited information from thick or multilayer clouds is available once the laser beam is attenuated.

b. Cloud radar MIRA-35. During the Arctic campaign Arctic Cloud Observations Using Airborne Measurements during Polar Day (ACLOUD)/Physical Feedbacks of Arctic Boundary Layer, Sea Ice, Cloud and Aerosol (PASCAL) in 2017 (Wendisch et al. 2019), OCEANET-Atmosphere was complemented for the first time with a vertically pointing motion-stabilized 35-GHz polarimetric Doppler cloud radar of type MIRA-35 (Görsdorf et al. 2015) in a separate housing. Because of the harsh environmental conditions of Antarctica, this Ka-band Doppler radar was installed into the OCEANET container for COALA. MIRA-35 uses a 1.2-m radar antenna which has been—also for weather protection—housed by an in-house-made aluminum/polycarbonate radome.

The moments derived from the Doppler spectra, such as radar reflectivity, vertical velocity, and spectral width, together with the linear depolarization ratio are used to characterize hydrometeors, ranging from cloud droplets and small ice crystals to precipitating snowflakes, drizzle, and weak rain (e.g., Bühl et al. 2016).

c. Doppler lidar LiTra-S. A Doppler lidar module LiTra-S (Abacus Laser) was installed in a heated custom-built housing next to the container for continuous measurements. Operating at a wavelength of 1.55 μm, it emits 320-ns pulses at a repetition rate of 10 kHz. For COALA, two rotatable wedged glass windows were installed on top of the transceiver unit to provide a scanning capability. The beam can be steered to off-zenith angles up to 7.5° and any azimuth direction. This setup enables the retrieval of horizontal wind profiles at any height where atmospheric targets (aerosol and clouds) are present (Päschke et al. 2015; Baars et al. 2023). Quasi-continuous vertical stare (elevation of 90°) observations are interrupted by a horizontal scan of 1-min duration every half hour. Height coverage of wind profiles is less

TABLE 1. Specification of the OCEANET-Atmosphere instrumentation during the deployment at Neumayer. More detailed information, including uncertainties, is given by Griesche et al. (2020).

Instrument Type (Reference)	Measured quantities	ν: frequency λ: wavelength R: vertical range	Temporal, vertical Resolution
Raman polarization lidar	Particle backscatter coefficient	$\lambda = 355, 532, 1064$ nm; R: 100–30 000 m	30 s–6 h, 7.5 m
Polly[XT]	Particle extinction coefficient	$\lambda = 355, 532$ nm; R: 300–30 000 m	1–6 h, 50–200 m
Engelmann et al. (2016)	Particle linear depolarization ratio	$\lambda = 355, 532$ nm; R: 100–30 000 m	30 s–6 h, 7.5 m
		($\lambda = 532$ nm: field of view 1 and 2 mrad)	
	Water vapor mixing ratio	$\lambda = 387, 407$ nm; R: 100–4000 m	30 s–10 min, 7.5 m
Microwave radiometer	Brightness temperature (TB)	$\nu = 22.24$–31.4 GHz	1 Hz
RPG HATPRO-G5		$\nu = 51.0$–58.0 GHz	
Rose et al. (2005), Walbröl et al. (2022)		R: column integral	
Doppler cloud radar	Radar reflectivity factor	$\nu = 35.5$ GHz; R: 150–13 000 m	2–10 s, 30 m
Metek MIRA-35	Linear depolarization ratio	$\nu = 35.5$ GHz; R: 150–13 000 m	2–10 s, 30 m
Görsdorf et al. (2015)	Hydrometeor vertical velocity	$\nu = 35.5$ GHz; R: 150–13 000 m	2–10 s, 30 m
Optical disdrometer	Particle size distribution	$\lambda = 880$ nm	30 s
OTT Parsivel[2]		R: 6 m	
Löffler-Mang and Joss (2000)		Size range 62 μm–24 mm	No. of bins: 32
Doppler lidar	Particle backscatter coefficient	$\lambda = 1.5\ \mu$m; R: 50–13 000 m	3.5 s, 48 m
Abacus LiTra-S	Vertical velocity	$\lambda = 1.5\ \mu$m; R: 50–13 000 m	3.5 s, 48 m
	Line-of-sight velocity (82.5° elev.)	$\lambda = 1.5\ \mu$m; R: 50–13 000 m	Every 30 min, 48 m
Sun, lunar, sky photometer	AOD and IWV	$\lambda = 340$–1640 nm	Variable
Cimel CE318-T		Column integral	
Barreto et al. (2016)			
SPC	Blowing snow particle size	$\lambda = 830$ nm	1 s
SPC-95		R: 10 cm	
Nishimura and Nemoto (2005)		Size range: 50–500 μm	No. of bins: 64

comprehensive compared to sites with less pristine aerosol conditions. Nonetheless, useful profiles can generally be derived from 50 m up to about 1 km. The heights above are only covered by the presence of cloud particles.

d. Microwave radiometer HATPRO. A 14-channel microwave radiometer (MWR) HATPRO (Rose et al. 2005) is part of the instrument set. The MWR HATPRO provides estimates of the liquid water path (LWP), integrated water vapor (IWV), as well as humidity and temperature profiles with a temporal resolution of 1 Hz. The MWR measures the emission of radiation from the atmosphere in two frequency bands ranging from 22.24 to 31.4 GHz and from 51.0 to 58.0 GHz at 14 different channels, based on which the column-integrated parameters and the profiles of humidity and temperature are retrieved using a neural network–based statistical approach, which was provided by the manufacturer for marine polar environments in the Northern Hemisphere. A cross-check with different regression retrievals revealed no significant differences for the LWP and IWV used in this study.

e. Photometer, disdrometer, snow particle counter, and surface snow samples. In addition to the remote sensing instruments, a sun/sky/lunar photometer (Cimel CE318-T) which has been modified with insulation and heating was installed at the roof of the container. The data are processed by the Aerosol Robotic Network (AERONET). During the polar night, observations

of the moon are used to derive the aerosol optical depth. An optical disdrometer (Parsivel[2], OTT company) for precipitation studies, basic meteorological sensors, a pyranometer, and a pyrgeometer for incoming short- and longwave (LW) radiation observations, as well as an all-sky camera for passive visible observations of the full sky, were installed as well. Approximately 30 m south of the container, a snow particle counter (SPC) and a snow trap were installed at 10 and 30 cm above the snow surface, respectively, to measure and sample blowing snow events. More details of the instrument and setup are described in Nishimura and Nemoto (2005) and Frey et al. (2020). Freshly fallen snow and blowing snow are collected for later chemical analysis in the vicinity of OCEANET-Atmosphere after significant snowfall or blowing snow events.

3. Neumayer observatories

The OCEANET-Atmosphere instruments are embedded in a framework of high-quality standard meteorological and air chemistry instruments and observations, which date back to the 1980s (König-Langlo and Loose 2007; Weller 2023a; Wesche et al. 2016). Both, the meteorological and the air chemistry observatory are part of the Global Atmosphere Watch network (Moreno 2023). From the extensive scientific program of the observatories, the following description will only touch on aspects of interest for this study.

The meteorological observatory collects standard meteorological parameters at a site 300 m southeast of the station (Fig. 1b), including temperature, humidity, and wind at 2- and 10-m height (Schmithüsen 2023). At this location, the upward and downward long- and shortwave fluxes are observed according to the standards of the Baseline Surface Radiation Network (Schmithüsen 2021). Routine radiosonde ascents are conducted daily at 1200 UTC, which are also fed into the Global Telecommunication System for model assimilation (Schmithüsen 2022b). Additionally, a ceilometer (Vaisala CL51) is mounted on the station roof and provides backscatter profiles at 910 nm (Schmithüsen 2022a).

The air chemistry observatory is installed approximately 1.5 km south of the actual station (Fig. 1b) to avoid local contamination. Ambient air is collected with a ventilated electropolished stainless steel inlet stack from a height of about 8 m above the surrounding snow surface. Sampling of aerosol and trace gases is performed offline in filters and flasks, as well as online in situ (for details, see Weller et al. 2011a,b; Weller 2023a). Filters are sampled with high- and low-volume flow for analysis of chemical composition, especially biweekly filters for analysis of INP concentrations are available (Gong et al. 2022; Wex et al. 2019). Online measurements of aerosol properties are available for total particle number, aerosol size distribution, scattering properties, and number of CCN. Additionally, snow accumulation is observed by reading stakes in the vicinity of the station.

4. Data assets

Data processing, dissemination, and analysis of the datasets from OCEANET-Atmosphere and auxiliary sources are performed in a layered architecture that is outlined in Fig. 2. While this section provides an overview, a more detailed description can be found in the appendix. The well-established (synergistic) Cloudnet algorithm (Illingworth et al. 2007; Tukiainen et al. 2020) and the PollyNET processing chain (Baars et al. 2016, 2017; Yin and Baars 2021) are the backbones of the data analysis. Retrieved data are made available either via the ACTRIS data portal (for data processed centrally at the cloud remote sensing data center unit) or general purpose databases (for data processed at the institute level). The latter one is usually the case for novel, higher-level retrievals.

The crucial link between the retrieved data and the scientific analysis is LARDA, a data cube which ties together all the different variables at different levels and provides easy, standardized access to the data (Radenz et al. 2022).
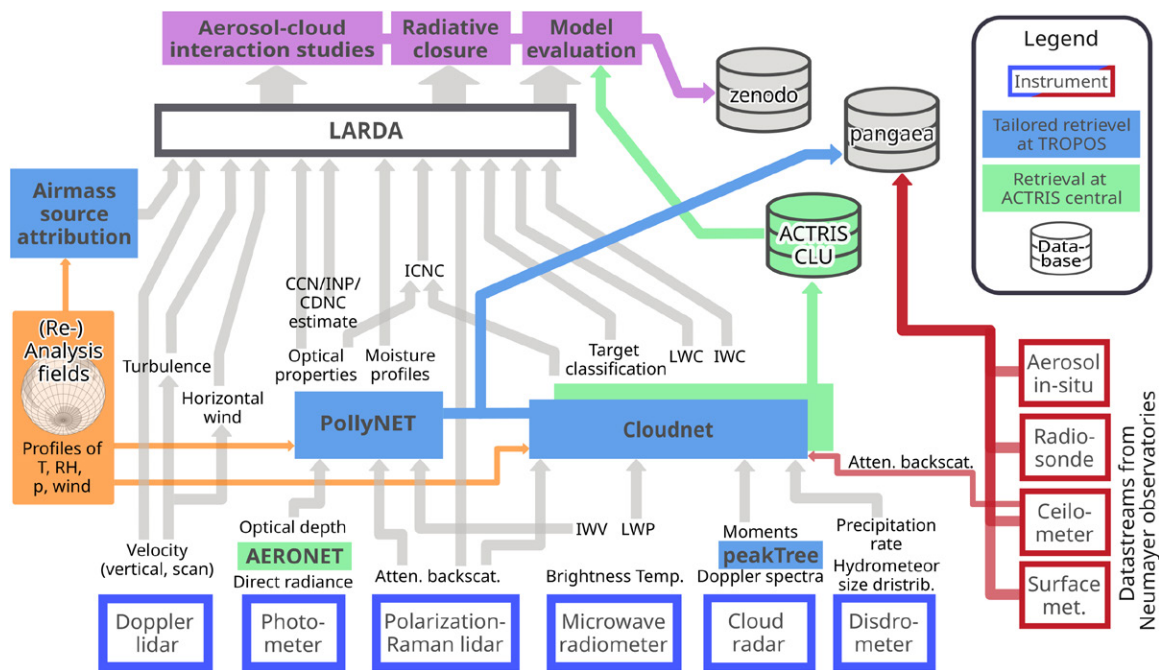
Fɪɢ. 2. Data flow from the instruments via synergistic retrievals to the scientific analysis. Abbreviations are temperature (*T*), pressure (*p*) ACTRIS Cloud Remote Sensing Data Centre (ACTRIS CLU), and ice crystal number concentration (ICNC). Further description is provided in the text.

5. Observational highlights from austral autumn and winter 2023

a. Aerosol–cloud interaction in shallow mixed-phase clouds. The radiative properties of a cloud are predominantly controlled by the amount of liquid that can be sustained at the cloud top despite the formation of ice at supercooled temperatures, acting as a sink for liquid water. Such a scenario was observed on 18 June 2023 when a mixed-phase cloud was present above Neumayer for almost 10 h where it was continuously captured by the remote sensing instrumentation (Fig. 3). Such cloud events are considered natural laboratories which serve as specimens for aerosol–cloud interaction studies (Morrison et al. 2012; Radenz et al. 2021b; Zhang et al. 2018), while their correct representation in large-scale models is still a challenge (Morrison et al. 2012). At the time of the event, Neumayer was meteorologically situated between a weakening low pressure system off the coast of eastern Dronning Maud Land, while a low-amplitude ridge over the Weddell Sea caused negligible pressure gradients in the area of the Ekström Ice Shelf. The cloud developed in a weak southeasterly to easterly flow. During the afternoon, the wind direction shifted toward the north, but wind velocity remained below 12 m s^{-1} (Fig. 3d). According to backward transport simulations, the cloud-carrying air masses resided only above water and ice surfaces without contact with midlatitude continental land for the previous 10 days. In this zonal flow, the IWV content remained low, at around 3.5 kg m^{-2}.

A supercooled liquid layer at cloud top was observed between 2- and 2.5-km height from 1240 to 2130 UTC. The presence of liquid water is corroborated by the presence of enhanced lidar backscatter values (Fig. 4c) and by the detection of elevated values of LWP (Fig. 4a) that are about 10 g m^2 above the slightly positively biased LWP observation from before the cloud event. The cloud-top temperature varied between −23° and −26°C. Ice sedimented from that liquid layer during the whole period. The lidar observations of the cloud-free atmosphere surrounding the cloud event reveal aerosol being present up to 3.2-km height during the whole day. A plume of hygroscopically grown aerosol particles was already observed at around 1000 UTC (dashed box in Figs. 3c,e) before the cloud appeared.
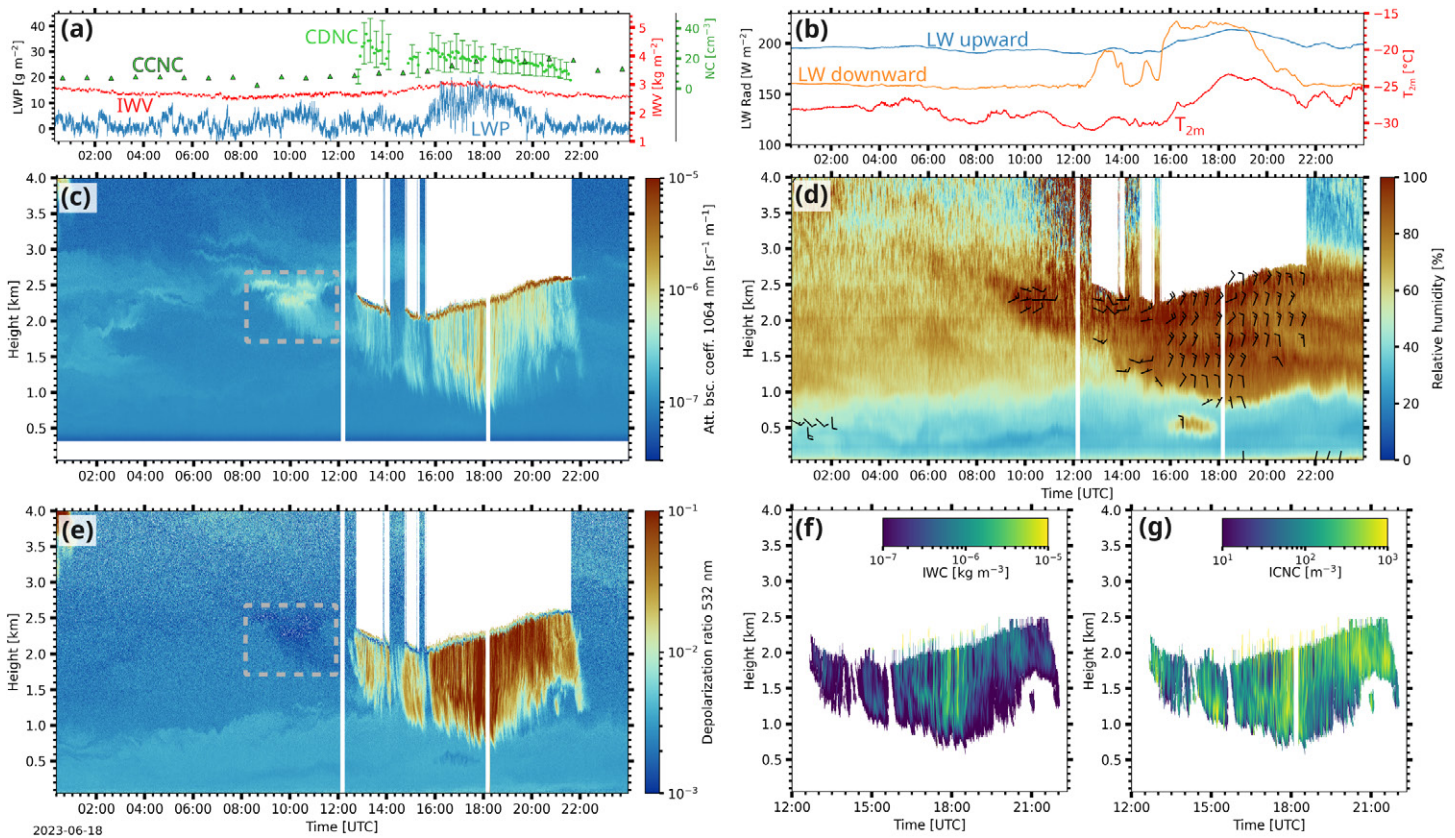
F<small>IG</small>. 3. **Mixed-phase cloud developing in a layer of marine aerosol on 18 Jun 2023. (a)** Time series of IWV, LWP, CCNC at a supersaturation of 0.2%, and CDNC 75 m above cloud base. **(b)** Time series of LW radiation and temperature at the surface. **(c)** Time–height cross section of lidar attenuated backscatter coefficient at 1064 nm. **(d)** RH with respect to liquid derived from the Raman water vapor channel and the Temp fields from ECMWFs IFS analysis and the wind barbs indicate wind direction and strength as observed by the scanning Doppler lidar. **(e)** Lidar volume linear depolarization ratio at 532 nm. **(f)** Time–height cross section of retrieved IWC. **(g)** Time–height cross section of retrieved ICNC. The dashed boxes in (c) and (e) indicate the plume of strong hygroscopic growth.

At the same time and height, profiles of relative humidity (RH) obtained from Polly^{XT} together with temperature fields from ECMWFs IFS analysis indicate peak values close to liquid saturation. Based on the anticorrelation of depolarization ratio at 532 nm and relative humidity, we presume that hygroscopic sea salt was present. Generally, the cloud formed in a moist layer, above roughly 0.5-km height, while the layer below remained comparably dry. At the cloud top, where the lidar backscatter indicates the supercooled liquid layer, relative humidity reached liquid saturation. At around 1800 UTC, a second, lower layer of high humidity was observed at 1.5–1.8-km height. In this slightly turbulent layer also, as indicated by the vertical velocity (not shown), additional secondary growth of the ice particles occurred, as can be inferred from the associated slight increase in the radar reflectivity factor (not shown).

The aerosol optical properties derived by the ground-based lidar, especially the inverse relation between depolarization ratio and humidity, point to sea salt aerosol being the predominant type, a conclusion which is in line with previous reports on free-tropospheric aerosol conditions over Eastern Antarctica during wintertime (Hara et al. 2011) and surface in situ observations at Neumayer (Weller et al. 2008, 2011a). The backscatter coefficient of the observed aerosol layers was overall below the detection limit of spaceborne lidars, such as CALIOP, which highlight the importance of high-quality ground-based observations for an appropriate assessment of aerosol–cloud interaction processes (Toth et al. 2018). Conversion of the aerosol optical properties into microphysical properties suggests
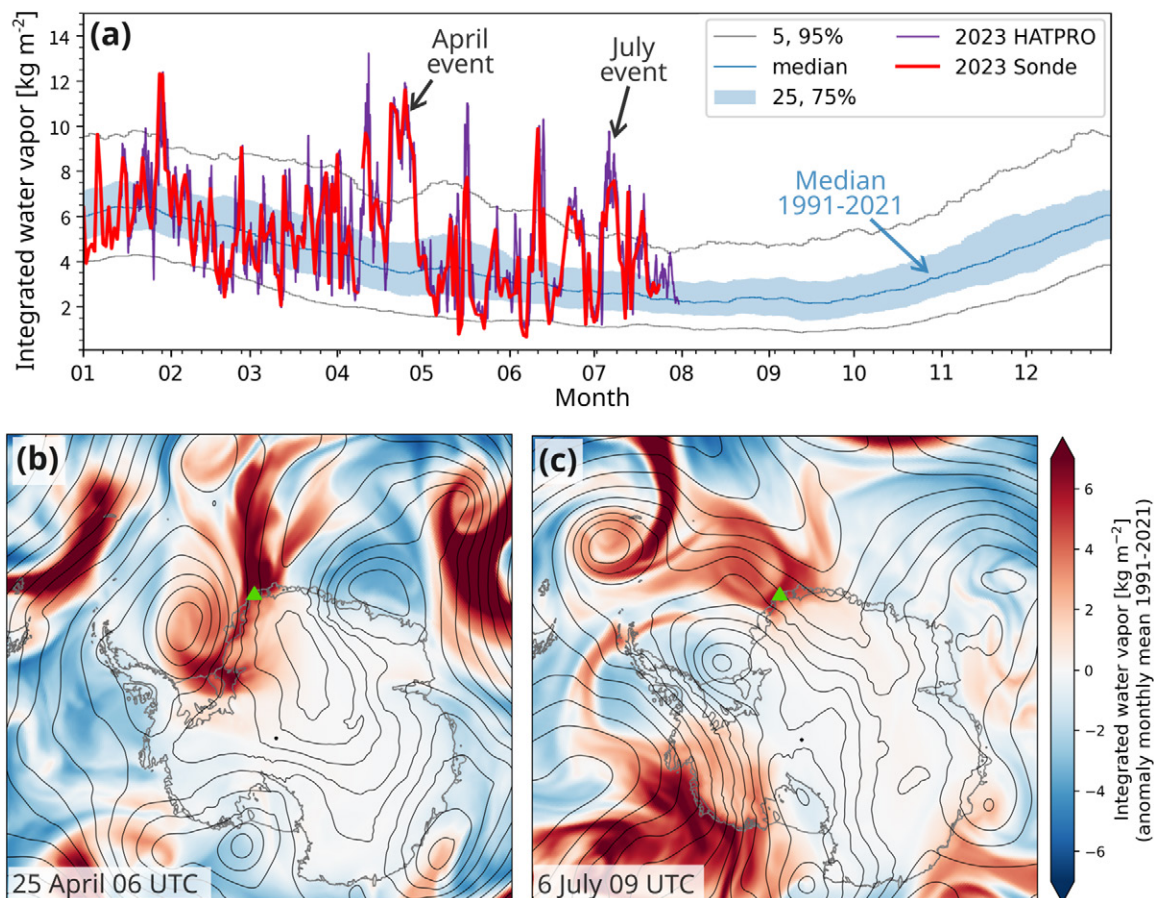
Fɪɢ. 4. Overview on annual cycle of IWV and anomalies for the two moist air intrusions. (a) Time series from daily radiosonde ascends and hourly mean derived from MWR HATPRO observations compared to daily climatology from radiosondes between 1991 and 2021. (b) ECMWFs ERA5 reanalysis on 0600 UTC 25 Apr 2023 with difference to April mean 1991–2021. (c) ECMWFs ERA5 reanalysis on 0900 UTC 6 Jul 2023 with a difference to July mean 1991–2021. Contours in (b) and (c) indicate a geopotential height of 700 hPa in intervals of 5 gpdm.

concentrations of CCN and INP in the order of $10–50\,cm^{-3}$ (at a supersaturation of 0.2%) and $10–100\,m^{-3}$, respectively. Cloud droplet number concentrations (CDNCs) derived from the lidar dual-field-of-view channels were between 20 and $50\,cm^{-3}$ with effective radii of $7–10\,\mu m$. The amount of ice sedimenting out of the liquid layer was about $1.0 \times 10^{-6}\,kg\,m^{-3}$ with a median number concentration of $150\,m^{-3}$ and a mean diameter of $260\,\mu m$ (with minimum size of ice particles in the retrieval of $1\,\mu m$). Hence, the concentrations of cloud-relevant aerosol particles match the concentrations of cloud droplets and ice crystals, respectively. While the virga itself dissolved in the dry layer, enhanced concentrations of hygroscopic aerosol were observed in situ at the surface between 1600 and 2100 UTC (Fig. 3a). Whether that increase is caused by residuals from the ice particles in the virga or the aerosol laden air being mixed to the surface remains open.

During the period of the mixed-phase cloud, the observed longwave downward radiation increased by up to $60\,W\,m^{-2}$ from the clear-sky value of $160\,W\,m^{-2}$. While the longwave balance was only close to zero in the beginning, after 1530 UTC, the cloud was thick enough to shift the balance to positive values close to $18\,W\,m^{-2}$. In response, the surface air temperature rose from −30° to −23°C. Spaceborne observations of the VIIRS onboard *NOAA-21* satellite during an overpass at 1930 UTC (not shown) revealed that the cloud covered almost the complete Ekström Ice Shelf before being advected further south, highlighting the regional extent of the radiative impact.

b. Warm air intrusions. Coastal Antarctica is subject to regular events of intrusions of warm and moist air masses from lower latitudes (e.g., Bromwich et al. 2020; Gorodetskaya et al. 2020). Derived from the 1991–2020 radiosounding dataset (Schmithüsen 2022b), roughly 3–14 high-moisture events usually occur per year at Neumayer. While the IWV content has a pronounced annual cycle, moist air intrusions occur throughout the year (Fig. 4a). In the following, we will present two cases in more detail that both exceeded the 95% percentile of the 30-yr climatology of IWV observed by radiosoundings. These cases do well represent the essential role of warm air intrusions for the mass balance of the ice shelf and the formation of supercooled liquid precipitation.

The first showcase, demonstrating intense snowfall production, was observed during the second half of April. An extensive low pressure system centered above the Weddell Sea advected exceptionally moist air masses from the Southern Ocean to the western Dronning Maud Land. Supported by moderate-to-strong meridional lower-tropospheric winds, these moist air masses were transported along the eastern coast of the Weddell Sea toward the Filchner–Ronne Ice Shelf and South Pole (Fig. 4b).

At Neumayer, IWV values above $8\,\mathrm{kg\,m^{-2}}$ with maxima of $12\,\mathrm{kg\,m^{-2}}$ were observed from 20 to 28 April 2023 (Fig. 5). Moderate snowfall was observed at the station almost continuously. The strongest precipitation, as indicated by high values of radar reflectivity factor, is associated with deep clouds, having top heights above 7-km height. During such periods, supercooled liquid water that is sustained in shallower mixed-phase clouds is depleted.
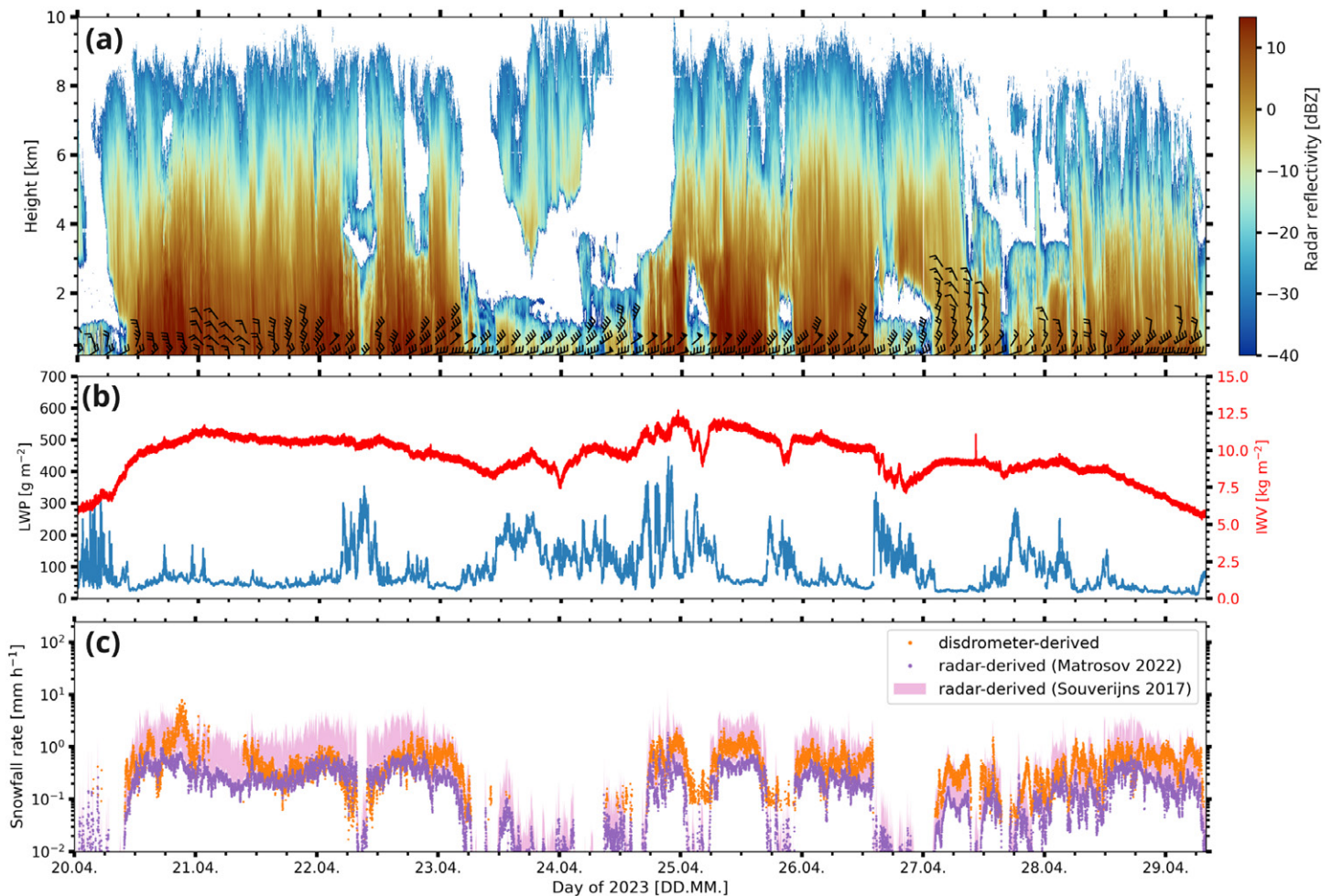

FIG. 5. Snowfall during the high IWV period from 20 to 28 Apr 2023. (a) Cloud radar reflectivity time–height cross section. Black wind barbs indicate wind direction and strength as observed by the scanning Doppler lidar downsampled to 3 h and 380 m. (b) IWV content and LWP derived from the MWR. (c) Snowfall rate (water equivalent) retrieved from the cloud radar reflectivity at 210 m and the disdrometer particle size distribution.

Under snowfall conditions, the scans of the Doppler lidar provide useful horizontal wind information up to 800–1300-m height. The northerly winds rarely dropped below 10 m s^{-1} in velocity and peaked above 30 m s^{-1}. Wind direction in the lowermost 200 m veered to east, due to terrain influence.

The amount of snow is quantified with the methodology presented by Matrosov et al. (2022) from the cloud radar and disdrometer observations. Cloud radar reflectivity Z at 210 m is converted into a snowfall rate S using the power-law relationship $Z = aS^b$ with the coefficient $a = 63$ and the exponent $b = 1.2$. Souverijns et al. (2017) suggest $a = 44$ for large particles, typical for coastal environments; $a = 7$ for small particles, typical for inland locations; and $b = 1.1$ for both. Following the Matrosov et al. (2022) approach, also for the Parsivel disdrometer observations, the raw counts are reprocessed with the mass–dimension power law $m = 0.03344 \star D^{1.9}$ (SI units). Rates of snow water equivalent precipitation ranged between 0.2 and 1.1 mm h^{-1} when deep clouds were present, giving an accumulated value of 41–86 mm as derived by radar and disdrometer, respectively. In general, these relationships between reflectivity and snowfall rate have an uncertainty of up to a factor of 2. Including additional cloud radar and disdrometer information will reduce the uncertainty in future studies. These estimates are also in agreement with the observed snow accumulation of roughly half a meter surrounding the station during the event. Under the absence of snow redistribution, this period would amount to more than 10% of the yearly snow accumulation observed at the northern part of the Ekström Ice Shelf (Rotschky et al. 2007).

The second noteworthy intrusion of warm and moist air masses took place during the polar night, from the afternoon on 4 July to the early morning of 9 July 2023 (Fig. 4c). The maximum IWV value of 10.1 kg m^{-2} was observed at 0520 UTC 6 July (Fig. 6d). Already since 2140 the day before, the 2-m temperature rose above −3°C (Fig. 6e). It remained above −5°C until 0115 UTC on 7 July. The maximum of −2.6°C marks the warmest temperature observed at Neumayer in July since the beginning of continuous observations in 1982. Such warm air masses also impacted cloud microphysics and precipitation formation. In the following, the discussion will focus on the period from 2200 UTC 5 July to 1200 UTC 6 July.
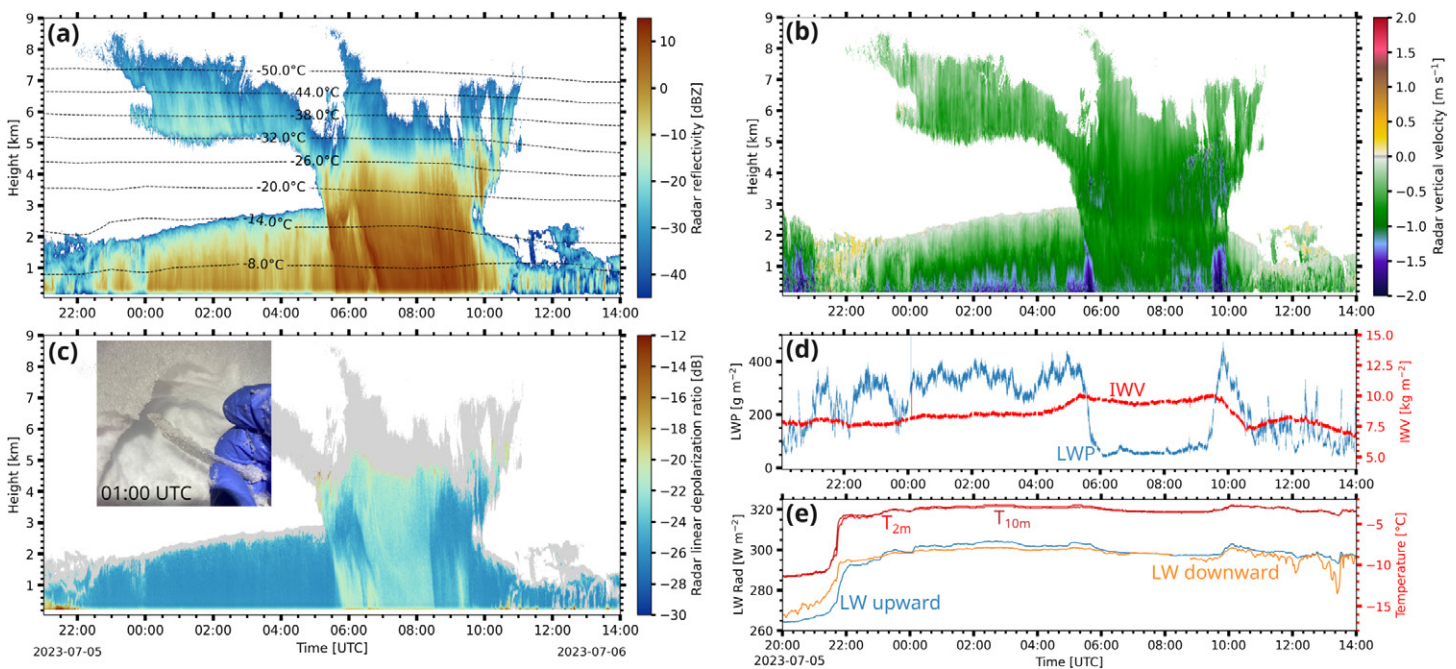

FIG. 6. Precipitation during the high IWV period from 5 to 6 Jul 2023. (a) Cloud radar reflectivity time–height cross section overlayed with temperature from ECMWFs IFS analysis. (b) Cloud radar vertical velocity. (c) Cloud radar linear depolarization ratio with inset picture showing the 2-mm ice layer on the surface at 0100 UTC. (d) Time series of IWV and LWP. (e) Time series of LW radiation and temperature at the surface.

Strong icing occurred on the in situ instrumentation, especially the Parsivel disdrometer, providing challenging conditions for all observations. Cloud radar observations show a shallow cloud between 2200 and 0530 UTC with the cloud top increasing from 2 to almost 3 km (Figs. 6a–c). Radar reflectivity and downward velocity increase with decreasing height peaking at 1.5 dBZ and –1.4 m s^{-1}, respectively. The liquid water path was above 200 g m^{-2}, peaking at 400 g m^{-2} (Fig. 6d).

The cloud radar's linear depolarization ratio remained low, close to the detection limit of –26 dB, indicating particles with a spherical cross section in their horizontal shape, i.e., supercooled drizzle. On the surface, a layer of clear ice accumulated atop snow fallen the day before. At 0100 UTC, the layer of ice was observed to be approximately 2-mm thick. After 0530 UTC, a vertically deeper precipitation system with cloud tops above 5 km and cloud-top temperatures below –32°C caused snow precipitation at the surface. Once the ice particles from aloft fell into the lower cloud layer, the liquid water path dropped to values below 60 g m^{-2}. By that time, the ice layer on the surface had almost doubled in thickness. The lidar was less affected by the icing but suffered signal attenuation in the lowest kilometer. However, during the discussed period, the observed volume depolarization ratio at 532 nm remained below 5%, while the values were close to 30% before 2200 and after 0540 UTC.

Concluding, no indications of solid precipitation were found in the period when cloud top height was below 3 km, making supercooled drizzle the most likely explanation for the observations. While supercooled drizzle has been observed in Antarctica before (Silber et al. 2019), no such observations on any ice shelf itself have been available so far.

c. Omnipresent stratospheric aerosol. While mostly pristine conditions are expected throughout the whole atmosphere in Antarctica (only sporadically interrupted by aerosol advection as, e.g., shown in the case of the free-tropospheric sea salt aerosol), the lidar observations revealed omnipresent aerosol layers in the stratosphere since the beginning of the observations in January 2023 (Fig. 7, top). Elevated backscatter coefficients are observed from below 9 km up to 17-km height, well above the tropopause level throughout the whole observational period. Separating the AOD to tropospheric and stratospheric contributions (Fig. 7, bottom left) by means of the lidar-derived extinction profile, it becomes clear that the stratospheric aerosol layers significantly contributed to the total AOD: while the troposphere was clean with pristine conditions of usually less than 0.03 (532 nm), the mean AOD in the stratosphere was 0.027 at 532 nm, and thus half of the observed total AOD. The observations from the lidar are in excellent agreement with unique AERONET lunar and solar AOD observations as shown in Fig. 7b. Total AOD ranged up to 0.08–0.09 in the visible wavelength range during the first half of 2023. The occurrence of polar stratospheric clouds (PSCs) at this time period and height range can be ruled out due to temperature regimes above –78°C (see contour lines in Fig. 7a). PSCs were sporadically observed since the end of May 2023, above 16-km height as shown in Figs. 7a and 7c. Thus, one can conclude that 50% of the total columnar AOD as observed with AERONET and other passive sensors was caused by stratospheric aerosol. The lidar-derived aerosol optical properties do clearly indicate sulfate aerosol, which is mainly caused by volcanic eruptions. The elevated AOD levels observed in the stratosphere since January 2023 are therefore most probably linked to the eruption of Hunga Tonga–Hunga Ha'apai in January 2022. During the eruption, large amounts of water vapor were injected together with respective aerosols and other precursor gases of volcanic origin, which can lead to sulfate aerosol formation (Legras et al. 2022; Lu et al. 2023). Compared to typical values in the absence of major eruptions (Kovilakam et al. 2020), the stratospheric AOD above Antarctica is increased by a factor of 3. Nonetheless, collocated measurements from the spaceborne lidar CALIOP did not identify any aerosol in its standard products. These significantly disturbed
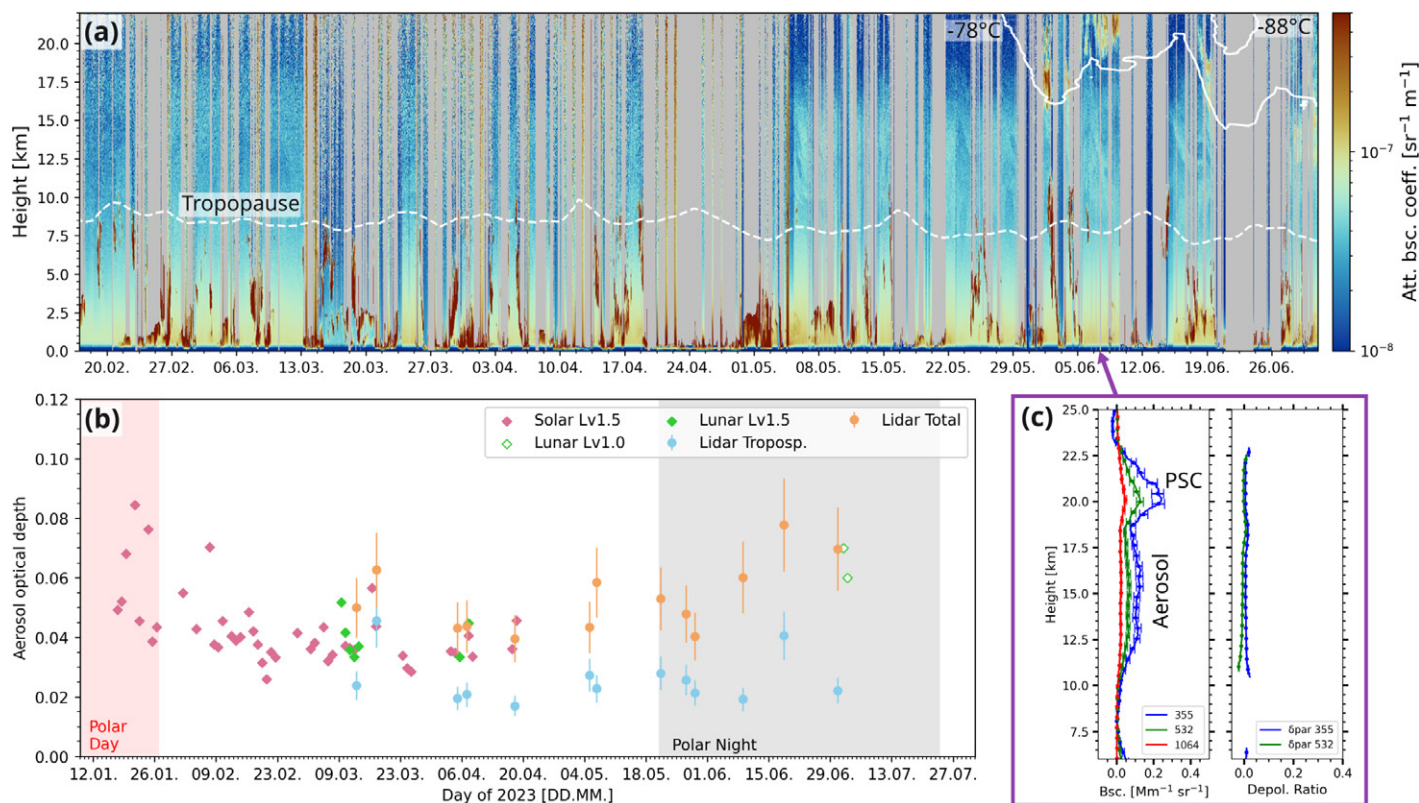
FIG. 7. Aerosol layers in the stratosphere. (a) Time–height cross section of attenuated backscatter coefficient at 1064 nm. Solid lines indicate Temp of −88° and −78°C, respectively; the dashed line indicates the approximate height of the tropopause. (b) Time series of AOD from lidar and photometer. (c) Profiles of optical properties obtained from the lidar observations with the Raman retrieval on 5 Jun 2023 from 1400 to 2230 UTC.

stratospheric background conditions may have influenced ozone depletion in the austral spring 2023, as shown by a perturbation by wildfire smoke after the Australian fires in 2020 (Ansmann et al. 2022). However, the troposphere, which is the main focus region for aerosol–cloud interaction, has been very clean and thus sensitive to occasional aerosol perturbations as presented in section 5a.

6. Summary and outlook

In January 2023, the OCEANET-Atmosphere observatory was deployed to Neumayer to obtain a 1-yr-covering snapshot of the cloud and aerosol conditions over the Ekström Ice Shelf in the Weddell Sea. The OCEANET-Atmosphere measurements constitute the first ground-based observations with collocated multiwavelength polarization lidar, cloud radar, microwave radiometer, and Doppler lidar in the Atlantic sector of Antarctica. To our knowledge, the only available similar dataset for Antarctica in wintertime was acquired at McMurdo Station during AWARE (Lubin et al. 2020), on the opposite side of the Antarctic continent. Based on the synergies of the measured set of parameters, comprehensive insights into the characteristics of atmospheric turbulence, aerosols, water vapor, clouds, and precipitation and their interaction were obtained. Thereby, processing and publication of the acquired datasets has been implemented by means of well-established and open platforms, such as ACTRIS Cloudnet, PollyNet, LARDA, AERONET, and the PANGAEA database. This approach ensures a sustained availability of the data. Further synergy is achieved by the availability of high-quality long-term records from the Neumayer observatories and the in situ samples of air and snow.

The aim of the COALA project, with its central component being the OCEANET-Atmosphere deployment at Neumayer, is to provide a thorough characterization of key processes of the

Antarctic climate system, including the vertical distribution of aerosols and their relevance for cloud processes, events of strong meridional transport of aerosol and moisture, and the structure of cloud and precipitation systems. In relation to these aims, representative observational examples were intensively discussed.

In one case study, we showed how hygroscopic marine aerosol, likely sea salt, in the lower free troposphere impacted cloud formation in mid-winter. The microphysical properties of a mixed-phase stratiform cloud that was formed in this aerosol were found to be controlled by the aerosol conditions, as the retrieved number concentrations of cloud droplets and ice crystals were in the same order as the concentration of CCN and INP. In such an aerosol-limited regime, minor perturbations in the aerosol load might lead to strong effects on cloud physics. The detailed observations during COALA allow for such closure studies, which provide a reference for evaluating future cloud-resolving modeling studies.

Since the start of the measurements, considerable, persistent amounts of aerosol were observed in the stratosphere. These stratospheric aerosol layers, which originated most likely from volcanic emissions of Hunga Tonga–Hunga Ha'apai, were found to contribute about 50% to the total atmospheric AOD. Despite being clearly identified in the ground-based observations, collocated measurements from the spaceborne lidar CALIOP did not identify any aerosol in its standard products. Such findings that cannot be obtained from passive observations highlight the importance of ground-based profiling observations for understanding aerosol–cloud interaction and ozone depletion in pristine environments.

Two exceptional events of warm air intrusions have been presented. One event caused snowfall equivalent to 10% of local annual accumulation within just a few days. Another event led to record July temperature maxima (since the observational record started in 1982) and the formation of a multihour period of supercooled drizzle confirmed visually by the growth of a 4-mm thick ice layer at the surface. Once that supercooled cloud was seeded with ice particles from above, the liquid was rapidly depleted. Future studies will for instance have to investigate 1) how the layer of solid ice, formed at the surface by the supercooled liquid precipitation, affected surface accumulation and mass balance of the ice shelf and 2) which effects the removal of water from the lower troposphere by the observed seeder–feeder processes has downstream. Neither of these processes have been satisfactorily observed above ice sheets in the past, highlighting the uniqueness of the collected dataset. Investigating the cloud processes under such warm and moist conditions is a pressing issue, as there is still debate about how the frequency and properties of atmospheric river events will change in a future climate (see also Wille et al. 2024a).

Given the 1-yr COALA dataset, future investigations can tackle the abovementioned key topics by means of thorough statistical evaluations. Ultimately, a reference dataset of the vertical structure of aerosol and clouds above the Ekström Ice Shelf is available, enabling future observational and modeling studies to improve the process understanding in the atmosphere of coastal Antarctica. Finally, it should be noted that the OCEANET-Atmosphere deployment to Neumayer constitutes only the starting point of an upcoming long-term time series of aerosol and cloud profiling observations at the site. At the beginning of 2024, the Alfred Wegner Institute extended the permanent observational capabilities at Neumayer with a 94-GHz cloud radar, a polarization lidar, and a scanning Doppler lidar, providing continuity from the initial COALA dataset. Thus, the long-term climatology of vertically resolved aerosol and cloud parameters at Neumayer continues.

Data availability statement. The Cloudnet datasets will be provided by the ACTRIS Data Centre node for cloud profiling (https://cloudnet.fmi.fi/site/neumayer). In the future, the Doppler lidar and PollyNET datasets will also be available via ACTRIS or PANGAEA. Meanwhile, they can be obtained upon request from the authors. Data from the Neumayer observatories will be available once per year via the respective PANGAEA collections (Schmithüsen 2023, 2021, 2022a,b; Weller 2023b). AERONET photometer observations are available from the AERONET database (http://aeronet.gsfc.nasa.gov/).

APPENDIX
Data Flow and Retrievals
The backbones of the data processing of the data provided by OCEANET-Atmosphere are the synergistic retrievals Cloudnet and PollyNET.

Cloudnet is the central processing chain of the CLU as part of ACTRIS and is operated at the Finnish Meteorological Institute. Retrieved are cloud macro- and microphysical properties from synergies between lidar, cloud radar, microwave radiometer, and disdrometer (Illingworth et al. 2007; Tukiainen et al. 2020). Default products of the Cloudnet algorithm are a target classification mask, providing an assessment on the presence and phase of cloud and aerosol particles, as well as estimates of liquid and ice water content. Cloudnet products from OCEANET-Atmosphere are processed by means of a twofold approach. Standardized processing is done at the CLU with the retrieved products published via the ACTRIS database. Novel, experimental retrievals, for example, tailored to low-level mixed-phase clouds (Griesche et al. 2020), the detection of multiple peaks in cloud radar Doppler spectra (Radenz et al. 2019), or for the detection of liquid water layers at ranges beyond lidar extinction (Schimmel et al. 2022), can be processed individually and published in general purpose databases such as PANGAEA.

The observations of the Polly^XT lidar are used to obtain profiles of aerosol optical properties. Quantities of interest are the particle backscatter coefficient, the particle extinction coefficient, and the particle linear depolarization ratio. Based on these optical properties, microphysical properties like the INP concentration can be inferred. The automated retrieval of optical properties is done with the PollyNET processing chain (Baars et al. 2016, 2017; Yin and Baars 2021), which is maintained by TROPOS. Together with the standardized setup and continuous measurements, this retrieval is one cornerstone of the PollyNET philosophy (Baars et al. 2016). Automated, continuous calibration of the lidar observations provides the basis for a plethora of products, comprising high-resolution, molecular-attenuation-corrected estimates of particle backscatter coefficients, water vapor products, and target classification. All operationally retrieved products are visualized (polly.tropos.de) in near–real time. Additionally, higher-level products can be derived offline from the lidar observations, such

as properties of the liquid phase in the cloud (Jimenez et al. 2020a,b) as well as the CCN concentration (CCNC) and the concentration of ICP (Mamouri and Ansmann 2016).

Retrieving properties of ice crystals, such as concentration and size, can be achieved by a combination of lidar and radar information (Delanoë and Hogan 2008; Mason et al. 2018; Sourdeval et al. 2018; Bühl et al. 2019). The results presented in section 5a were derived with the variational approach cloud, aerosol, and precipitation from multiple instruments using a variational technique (CAPTIVATE; Mason et al. 2017, 2018, 2023). However, well-calibrated and quality-controlled input data are required, which are provided by Cloudnet and PollyNET.

Additional information on airmass history is included in the data analysis by a time–height resolved dataset derived from airmass transport simulations (Radenz et al. 2021a). For this product, 10-day backward simulations were initialized every 3 h every 500 m up to 12-km height.

As mentioned in section 4, the data are accessed for scientific analysis with the LARDA data cube (Radenz et al. 2022). Any analyzed data or statistics might then also be published in appropriate databases.

References

Adhikari, L., Z. Wang, and M. Deng, 2012: Seasonal variations of Antarctic clouds observed by CloudSat and CALIPSO satellites. *J. Geophys. Res.*, **117**, D04202, https://doi.org/10.1029/2011JD016719.

Alexander, S. P., A. Protat, A. Berne, and L. Ackermann, 2023: Radar-derived snowfall microphysical properties at Davis, Antarctica. *J. Geophys. Res. Atmos.*, **128**, e2022JD038389, https://doi.org/10.1029/2022JD038389.

Ansmann, A., and Coauthors, 2022: Ozone depletion in the Arctic and Antarctic stratosphere induced by wildfire smoke. *Atmos. Chem. Phys.*, **22**, 11701–11726, https://doi.org/10.5194/acp-22-11701-2022.

Baars, H., and Coauthors, 2012: Aerosol profiling with lidar in the Amazon basin during the wet and dry season. *J. Geophys. Res.*, **117**, D21201, https://doi.org/10.1029/2012JD018338.

——, and Coauthors, 2016: An overview of the first decade of PollyNET: An emerging network of automated Raman-polarization lidars for continuous aerosol profiling. *Atmos. Chem. Phys.*, **16**, 5111–5137, https://doi.org/10.5194/acp-16-5111-2016.

——, P. Seifert, R. Engelmann, and U. Wandinger, 2017: Target categorization of aerosol and clouds by continuous multiwavelength-polarization lidar measurements. *Atmos. Meas. Tech.*, **10**, 3175–3201, https://doi.org/10.5194/amt-10-3175-2017.

——, and Coauthors, 2023: Long-term validation of Aeolus L2B wind products at Punta Arenas, Chile, and Leipzig, Germany. *Atmos. Meas. Tech.*, **16**, 3809–3834, https://doi.org/10.5194/amt-16-3809-2023.

Barreto, Á., and Coauthors, 2016: The new sun-sky-lunar Cimel CE318-T multiband photometer—A comprehensive performance evaluation. *Atmos. Meas. Tech.*, **9**, 631–654, https://doi.org/10.5194/amt-9-631-2016.

Block, K., F. A. Schneider, J. Mülmenstädt, M. Salzmann, and J. Quaas, 2020: Climate models disagree on the sign of total radiative feedback in the Arctic. *Tellus*, **72A**, 1696139, https://doi.org/10.1080/16000870.2019.1696139.

Bohlmann, S., H. Baars, M. Radenz, R. Engelmann, and A. Macke, 2018: Ship-borne aerosol profiling with lidar over the Atlantic Ocean: From pure marine conditions to complex dust–smoke mixtures. *Atmos. Chem. Phys.*, **18**, 9661–9679, https://doi.org/10.5194/acp-18-9661-2018.

Bracegirdle, T. J., G. Krinner, M. Tonelli, F. A. Haumann, K. A. Naughten, T. Rackow, L. A. Roach, and I. Wainer, 2020: Twenty first century changes in Antarctic and Southern Ocean surface climate in CMIP6. *Atmos. Sci. Lett.*, **21**, e984, https://doi.org/10.1002/asl.984.

Bromwich, D. H., and Coauthors, 2012: Tropospheric clouds in Antarctica. *Rev. Geophys.*, **50**, RG1004, https://doi.org/10.1029/2011RG000363.

——, and Coauthors, 2020: The Year of Polar Prediction in the Southern Hemisphere (YOPP-SH). *Bull. Amer. Meteor. Soc.*, **101**, E1653–E1676, https://doi.org/10.1175/BAMS-D-19-0255.1.

Bühl, J., P. Seifert, A. Myagkov, and A. Ansmann, 2016: Measuring ice- and liquid-water properties in mixed-phase cloud layers at the Leipzig Cloudnet station. *Atmos. Chem. Phys.*, **16**, 10609–10620, https://doi.org/10.5194/acp-16-10609-2016.

——, ——, M. Radenz, H. Baars, and A. Ansmann, 2019: Ice crystal number concentration from lidar, cloud radar and radar wind profiler measurements. *Atmos. Meas. Tech.*, **12**, 6601–6617, https://doi.org/10.5194/amt-12-6601-2019.

Clem, K. R., R. L. Fogt, J. Turner, B. R. Lintner, G. J. Marshall, J. R. Miller, and J. A. Renwick, 2020: Record warming at the South Pole during the past three decades. *Nat. Climate Change*, **10**, 762–770, https://doi.org/10.1038/s41558-020-0815-z.

Dai, G., and Coauthors, 2018: Calibration of Raman lidar water vapor profiles by means of AERONET photometer observations and GDAS meteorological data. *Atmos. Meas. Tech.*, **11**, 2735–2748, https://doi.org/10.5194/amt-11-2735-2018.

Delanoë, J., and R. J. Hogan, 2008: A variational scheme for retrieving ice cloud properties from combined radar, lidar, and infrared radiometer. *J. Geophys. Res.*, **113**, D07204, https://doi.org/10.1029/2007JD009000.

Engelmann, R., and Coauthors, 2016: The automated multiwavelength Raman polarization and water-vapor lidar PollyXT: The neXT generation. *Atmos. Meas. Tech.*, **9**, 1767–1784, https://doi.org/10.5194/amt-9-1767-2016.

——, and Coauthors, 2021: Wildfire smoke, Arctic haze, and aerosol effects on mixed-phase and cirrus clouds over the North Pole region during MOSAiC: An introduction. *Atmos. Chem. Phys.*, **21**, 13397–13423, https://doi.org/10.5194/acp-21-13397-2021.

Floutsi, A. A., and Coauthors, 2023: DeLiAn—A growing collection of depolarization ratio, lidar ratio and Ångström exponent for different aerosol types and mixtures from ground-based lidar observations. *Atmos. Meas. Tech.*, **16**, 2353–2379, https://doi.org/10.5194/amt-16-2353-2023.

Francis, D., K. S. Mattingly, M. Temimi, R. Massom, and P. Heil, 2020: On the crucial role of atmospheric rivers in the two major Weddell Polynya events in 1973 and 2017 in Antarctica. *Sci. Adv.*, **6**, eabc2695, https://doi.org/10.1126/sciadv.abc2695.

Franklin, C. N., Z. Sun, D. Bi, M. Dix, H. Yan, and A. Bodas-Salcedo, 2013: Evaluation of clouds in ACCESS using the satellite simulator package COSP: Global, seasonal, and regional cloud properties. *J. Geophys. Res. Atmos.*, **118**, 732–748, https://doi.org/10.1029/2012JD018469.

Frey, M. M., and Coauthors, 2020: First direct observation of sea salt aerosol production from blowing snow above sea ice. *Atmos. Chem. Phys.*, **20**, 2549–2578, https://doi.org/10.5194/acp-20-2549-2020.

Ghiz, M. L., R. C. Scott, A. M. Vogelmann, J. T. M. Lenaerts, M. Lazzara, and D. Lubin, 2021: Energetics of surface melt in West Antarctica. *Cryosphere*, **15**, 3459–3494, https://doi.org/10.5194/tc-15-3459-2021.

Gong, X., and Coauthors, 2022: Significant continental source of ice-nucleating particles at the tip of Chile's southernmost Patagonia region. *Atmos. Chem. Phys.*, **22**, 10505–10525, https://doi.org/10.5194/acp-22-10505-2022.

Gorodetskaya, I. V., T. Silva, H. Schmithüsen, and N. Hirasawa, 2020: Atmospheric river signatures in radiosonde profiles and reanalyses at the Dronning Maud Land Coast, East Antarctica. *Adv. Atmos. Sci.*, **37**, 455–476, https://doi.org/10.1007/s00376-020-9221-8.

Görsdorf, U., V. Lehmann, M. Bauer-Pfundstein, G. Peters, D. Vavriv, V. Vinogradov, and V. Volkov, 2015: A 35-GHz polarimetric Doppler radar for long-term observations of cloud parameters—Description of system and data processing. *J. Atmos. Oceanic Technol.*, **32**, 675–690, https://doi.org/10.1175/JTECH-D-14-00066.1.

Grazioli, J., C. Genthon, B. Boudevillain, C. Duran-Alarcon, M. Del Guasta, J.-B. Madeleine, and A. Berne, 2017: Measurements of precipitation in Dumont d'Urville, Adélie Land, East Antarctica. *Cryosphere*, **11**, 1797–1811, https://doi.org/10.5194/tc-11-1797-2017.

Griesche, H. J., and Coauthors, 2020: Application of the shipborne remote sensing supersite OCEANET for profiling of Arctic aerosols and clouds during *Polarstern* cruise PS106. *Atmos. Meas. Tech.*, **13**, 5335–5358, https://doi.org/10.5194/amt-13-5335-2020.

——, K. Ohneiser, P. Seifert, M. Radenz, R. Engelmann, and A. Ansmann, 2021: Contrasting ice formation in Arctic clouds: Surface-coupled vs. surface-decoupled clouds. *Atmos. Chem. Phys.*, **21**, 10357–10374, https://doi.org/10.5194/acp-21-10357-2021.

——, C. Barrientos-Velasco, H. Deneke, A. Hünerbein, P. Seifert, and A. Macke, 2024: Low-level Arctic clouds: A blind zone in our knowledge of the radiation budget. *Atmos. Chem. Phys.*, **24**, 597–612, https://doi.org/10.5194/acp-24-597-2024.

Grosvenor, D. P., and R. Wood, 2014: The effect of solar zenith angle on MODIS cloud optical and microphysical retrievals within marine liquid water clouds. *Atmos. Chem. Phys.*, **14**, 7291–7321, https://doi.org/10.5194/acp-14-7291-2014.

Hara, K., K. Osada, C. Nishita-Hara, and T. Yamanouchi, 2011: Seasonal variations and vertical features of aerosol particles in the Antarctic troposphere. *Atmos. Chem. Phys.*, **11**, 5471–5484, https://doi.org/10.5194/acp-11-5471-2011.

——, M. Hayashi, M. Yabuki, M. Shiobara, and C. Nishita-Hara, 2014: Simultaneous aerosol measurements of unusual aerosol enhancement in the troposphere

over Syowa Station, Antarctica. *Atmos. Chem. Phys.*, **14**, 4169–4183, https://doi.org/10.5194/acp-14-4169-2014.

Hartmann, M., and Coauthors, 2020: Wintertime airborne measurements of ice nucleating particles in the high Arctic: A hint to a marine, biogenic source for ice nucleating particles. *Geophys. Res. Lett.*, **47**, e2020GL087770, https://doi.org/10.1029/2020GL087770.

Hyder, P., and Coauthors, 2018: Critical Southern Ocean climate model biases traced to atmospheric model cloud errors. *Nat. Commun.*, **9**, 3625, https://doi.org/10.1038/s41467-018-05634-2.

Illingworth, A. J., and Coauthors, 2007: Cloudnet: Continuous evaluation of cloud profiles in seven operational models using ground-based observations. *Bull. Amer. Meteor. Soc.*, **88**, 883–898, https://doi.org/10.1175/BAMS-88-6-883.

Jimenez, C., A. Ansmann, R. Engelmann, D. Donovan, A. Malinka, J. Schmidt, P. Seifert, and U. Wandinger, 2020a: The dual-field-of-view polarization lidar technique: A new concept in monitoring aerosol effects in liquid-water clouds—Theoretical framework. *Atmos. Chem. Phys.*, **20**, 15 247–15 263, https://doi.org/10.5194/acp-20-15247-2020.

——, and Coauthors, 2020b: The dual-field-of-view polarization lidar technique: A new concept in monitoring aerosol effects in liquid-water clouds—Case studies. *Atmos. Chem. Phys.*, **20**, 15 265–15 284, https://doi.org/10.5194/acp-20-15265-2020.

Kanitz, T., A. Ansmann, R. Engelmann, and D. Althausen, 2013a: North-south cross sections of the vertical aerosol distribution over the Atlantic Ocean from multiwavelength Raman/polarization lidar during Polarstern cruises. *J. Geophys. Res. Atmos.*, **118**, 2643–2655, https://doi.org/10.1002/jgrd.50273.

——, ——, P. Seifert, R. Engelmann, J. Kalisch, and D. Althausen, 2013b: Radiative effect of aerosols above the northern and southern Atlantic Ocean as determined from shipborne lidar observations. *J. Geophys. Res. Atmos.*, **118**, 12 556–12 565, https://doi.org/10.1002/2013JD019750.

König-Langlo, G., and B. Loose, 2007: The meteorological observatory at Neumayer Stations (GvN and NM-II) Antarctica. *Polarforschung*, **76**, 25–38, https://doi.org/10.2312/POLARFORSCHUNG.76.1-2.25.

Kovilakam, M., L. W. Thomason, N. Ernest, L. Rieger, A. Bourassa, and L. Millán, 2020: The Global Space-based Stratospheric Aerosol Climatology (version 2.0): 1979–2018. *Earth Syst. Sci. Data*, **12**, 2607–2634, https://doi.org/10.5194/essd-12-2607-2020.

Lachlan-Cope, T., C. Listowski, and S. O'Shea, 2016: The microphysics of clouds over the Antarctic Peninsula – Part I: Observations. *Atmos. Chem. Phys.*, **16**, 15 605–15 617, https://doi.org/10.5194/acp-16-15605-2016.

Laj, P., and Coauthors, 2024: Aerosol, Clouds and Trace Gases Research Infrastructure (ACTRIS): The European research infrastructure supporting atmospheric science. *Bull. Amer. Meteor. Soc.*, **105**, E1098–E1136, https://doi.org/10.1175/BAMS-D-23-0064.1.

Legras, B., and Coauthors, 2022: The evolution and dynamics of the Hunga Tonga–Hunga Ha'apai sulfate aerosol plume in the stratosphere. *Atmos. Chem. Phys.*, **22**, 14 957–14 970, https://doi.org/10.5194/acp-22-14957-2022.

Listowski, C., J. Delanoë, A. Kirchgaessner, T. Lachlan-Cope, and J. King, 2019: Antarctic clouds, supercooled liquid water and mixed phase, investigated with DARDAR: Geographical and seasonal variations. *Atmos. Chem. Phys.*, **19**, 6771–6808, https://doi.org/10.5194/acp-19-6771-2019.

Löffler-Mang, M., and J. Joss, 2000: An optical disdrometer for measuring size and velocity of hydrometeors. *J. Atmos. Oceanic Technol.*, **17**, 130–139, https://doi.org/10.1175/1520-0426(2000)017<0130:AODFMS>2.0.CO;2.

Lu, J., and Coauthors, 2023: Stratospheric aerosol and ozone responses to the Hunga Tonga-Hunga Ha'apai volcanic eruption. *Geophys. Res. Lett.*, **50**, e2022GL102315, https://doi.org/10.1029/2022GL102315.

Lubin, D., and Coauthors, 2020: AWARE: The Atmospheric Radiation Measurement (ARM) West Antarctic Radiation Experiment. *Bull. Amer. Meteor. Soc.*, **101**, E1069–E1091, https://doi.org/10.1175/BAMS-D-18-0278.1.

Maahn, M., C. Burgard, S. Crewell, I. V. Gorodetskaya, S. Kneifel, S. Lhermitte, K. Van Tricht, and N. P. M. Van Lipzig, 2014: How does the spaceborne radar blind zone affect derived surface snowfall statistics in polar regions? *J. Geophys. Res. Atmos.*, **119**, 13 604–13 620, https://doi.org/10.1002/2014JD022079.

Mace, G. G., and Coauthors, 2021: Southern ocean cloud properties derived from CAPRICORN and MARCUS data. *J. Geophys. Res. Atmos.*, **126**, e2020JD033368, https://doi.org/10.1029/2020JD033368.

Mallet, M. D., and Coauthors, 2023: Untangling the influence of Antarctic and Southern Ocean life on clouds. *Elementa*, **11**, 00130, https://doi.org/10.1525/elementa.2022.00130.

Mamouri, R.-E., and A. Ansmann, 2016: Potential of polarization lidar to provide profiles of CCN- and INP-relevant aerosol parameters. *Atmos. Chem. Phys.*, **16**, 5905–5931, https://doi.org/10.5194/acp-16-5905-2016.

Mason, S. L., J. C. Chiu, R. J. Hogan, and L. Tian, 2017: Improved rain rate and drop size retrievals from airborne Doppler radar. *Atmos. Chem. Phys.*, **17**, 11 567–11 589, https://doi.org/10.5194/acp-17-11567-2017.

——, C. J. Chiu, R. J. Hogan, D. Moisseev, and S. Kneifel, 2018: Retrievals of riming and snow density from vertically pointing Doppler radars. *J. Geophys. Res. Atmos.*, **123**, 13 807–13 834, https://doi.org/10.1029/2018JD028603.

——, R. J. Hogan, A. Bozzo, and N. L. Pounder, 2023: A unified synergistic retrieval of clouds, aerosols, and precipitation from EarthCARE: The ACM-CAP product. *Atmos. Meas. Tech.*, **16**, 3459–3486, https://doi.org/10.5194/amt-16-3459-2023.

Matrosov, S. Y., M. D. Shupe, and T. Uttal, 2022: High temporal resolution estimates of Arctic snowfall rates emphasizing gauge and radar-based retrievals from the MOSAiC expedition. *Elementa*, **10**, 00101, https://doi.org/10.1525/elementa.2021.00101.

Mayewski, P. A., and Coauthors, 2009: State of the Antarctic and Southern Ocean climate system. *Rev. Geophys.*, **47**, RG1003, https://doi.org/10.1029/2007RG000231.

Mewes, D., and C. Jacobi, 2019: Heat transport pathways into the Arctic and their connections to surface air temperatures. *Atmos. Chem. Phys.*, **19**, 3927–3937, https://doi.org/10.5194/acp-19-3927-2019.

Moreno, S., 2023: The WMO Global Atmosphere Watch Programme new implementation plan and strategic objectives. *EGU General Assembly 2023*, Vienna, Austria, European Geosciences Union, EGU23-14442, https://doi.org/10.5194/egusphere-egu23-14442.

Morrison, H., G. de Boer, G. Feingold, J. Harrington, M. D. Shupe, and K. Sulia, 2012: Resilience of persistent Arctic mixed-phase clouds. *Nat. Geosci.*, **5**, 11–17, https://doi.org/10.1038/ngeo1332.

Müller, D., U. Wandinger, and A. Ansmann, 1999: Microphysical particle parameters from extinction and backscatter lidar data by inversion with regularization: Theory. *Appl. Opt.*, **38**, 2346–2357, https://doi.org/10.1364/AO.38.002346.

——, A. Ansmann, I. Mattis, M. Tesche, U. Wandinger, D. Althausen, and G. Pisani, 2007: Aerosol-type-dependent lidar ratios observed with Raman lidar. *J. Geophys. Res.*, **112**, D16202, https://doi.org/10.1029/2006JD008292.

Nicolas, J. P., and D. H. Bromwich, 2011: Climate of West Antarctica and influence of marine air intrusions. *J. Climate*, **24**, 49–67, https://doi.org/10.1175/2010JCLI3522.1.

Nishimura, K., and M. Nemoto, 2005: Blowing snow at Mizuho station, Antarctica. *Philos. Trans. Roy. Soc.*, **A363**, 1647–1662, https://doi.org/10.1098/rsta.2005.1599.

Päschke, E., R. Leinweber, and V. Lehmann, 2015: An assessment of the performance of a 1.5 μm Doppler lidar for operational vertical wind profiling based on a 1-year trial. *Atmos. Meas. Tech.*, **8**, 2251–2266, https://doi.org/10.5194/amt-8-2251-2015.

Radenz, M., J. Bühl, P. Seifert, H. Griesche, and R. Engelmann, 2019: peakTree: A framework for structure-preserving radar Doppler spectra analysis. *Atmos. Meas. Tech.*, **12**, 4813–4828, https://doi.org/10.5194/amt-12-4813-2019.

——, P. Seifert, H. Baars, A. A. Floutsi, Z. Yin, and J. Bühl, 2021a: Automated time–height-resolved air mass source attribution for profiling remote sensing applications. *Atmos. Chem. Phys.*, **21**, 3015–3033, https://doi.org/10.5194/acp-21-3015-2021.

——, and Coauthors, 2021b: Hemispheric contrasts in ice formation in stratiform mixed-phase clouds: Disentangling the role of aerosol and dynamics with ground-based remote sensing. *Atmos. Chem. Phys.*, **21**, 17 969–17 994, https://doi.org/10.5194/acp-21-17969-2021.

——, J. Bühl, W. Schimmel, T. Vogl, J. Röttenbacher, and M. Lochmann, 2022: Lacros-tropos/larda: Larda v3.3.5. Zenodo, accessed 28 May 2024, https://doi.org/10.5281/ZENODO.8337354.

Rose, T., S. Crewell, U. Löhnert, and C. Simmer, 2005: A network suitable microwave radiometer for operational monitoring of the cloudy atmosphere. *Atmos. Res.*, **75**, 183–200, https://doi.org/10.1016/j.atmosres.2004.12.005.

Rotschky, G., P. Holmlund, E. Isaksson, R. Mulvaney, H. Oerter, M. R. Van Den Broeke, and J.-G. Winther, 2007: A new surface accumulation map for western Dronning Maud Land, Antarctica, from interpolation of point measurements. *J. Glaciol.*, **53**, 385–398, https://doi.org/10.3189/002214307783258459.

Salzmann, M., 2017: The polar amplification asymmetry: Role of Antarctic surface height. *Earth Syst. Dyn.*, **8**, 323–336, https://doi.org/10.5194/esd-8-323-2017.

Schimmel, W., H. Kalesse-Los, M. Maahn, T. Vogl, A. Foth, P. S. Garfias, and P. Seifert, 2022: Identifying cloud droplets beyond lidar attenuation from vertically pointing cloud radar observations using artificial neural networks. *Atmos. Meas. Tech.*, **15**, 5343–5366, https://doi.org/10.5194/amt-15-5343-2022.

Schmithüsen, H., 2021: Basic and other measurements of radiation at Neumayer Station (1992-04 et seq). 358 datasets, accessed 31 August 2023, https://doi.org/10.1594/PANGAEA.932418.

——, 2022a: Ceilometer raw data measured at Neumayer Station (2009-02 et seq). 156 datasets, accessed 31 August 2023, https://doi.org/10.1594/PANGAEA.952482.

——, 2022b: Radiosonde measurements from Neumayer Station (1983-02 et seq). 451 datasets, accessed 31 August 2023, https://doi.org/10.1594/PANGAEA.940584.

——, 2023: Continuous meteorological observations at Neumayer station (1982-03 et seq). Accessed 18 January 2024, https://doi.org/10.1594/PANGAEA.962313.

Scott, R. C., D. Lubin, A. M. Vogelmann, and S. Kato, 2017: West Antarctic ice sheet cloud cover and surface radiation budget from NASA A-Train satellites. *J. Climate*, **30**, 6151–6170, https://doi.org/10.1175/JCLI-D-16-0644.1.

Seifert, P., and Coauthors, 2015: Seasonal variability of heterogeneous ice formation in stratiform clouds over the Amazon basin. *Geophys. Res. Lett.*, **42**, 5587–5593, https://doi.org/10.1002/2015GL064068.

Shupe, M. D., and Coauthors, 2022: Overview of the MOSAiC expedition: Atmosphere. *Elementa*, **10**, 00060, https://doi.org/10.1525/elementa.2021.00060.

Silber, I., and Coauthors, 2019: Persistent supercooled drizzle at temperatures below −25°C observed at McMurdo Station, Antarctica. *J. Geophys. Res. Atmos.*, **124**, 10878–10895, https://doi.org/10.1029/2019JD030882.

Sourdeval, O., E. Gryspeerdt, M. Krämer, T. Goren, J. Delanoë, A. Afchine, F. Hemmer, and J. Quaas, 2018: Ice crystal number concentration estimates from lidar–radar satellite remote sensing—Part I: Method and evaluation. *Atmos. Chem. Phys.*, **18**, 14327–14350, https://doi.org/10.5194/acp-18-14327-2018.

Souverijns, N., A. Gossart, S. Lhermitte, I. Gorodetskaya, S. Kneifel, M. Maahn, F. Bliven, and N. Van Lipzig, 2017: Estimating radar reflectivity—Snowfall rate relationships and their uncertainties over Antarctica by combining disdrometer and radar observations. *Atmos. Res.*, **196**, 211–223, https://doi.org/10.1016/j.atmosres.2017.06.001.

Stammerjohn, S. E., and T. A. Scambos, 2020: Warming reaches the South Pole. *Nat. Climate Change*, **10**, 710–711, https://doi.org/10.1038/s41558-020-0827-8.

Toth, T. D., J. R. Campbell, J. S. Reid, J. L. Tackett, M. A. Vaughan, J. Zhang, and J. W. Marquis, 2018: Minimum aerosol layer detection sensitivities and their subsequent impacts on aerosol optical thickness retrievals in CALIPSO level 2 data products. *Atmos. Meas. Tech.*, **11**, 499–514, https://doi.org/10.5194/amt-11-499-2018.

Trenberth, K. E., and J. T. Fasullo, 2010: Simulation of present-day and twenty-first-century energy budgets of the Southern Oceans. *J. Climate*, **23**, 440–454, https://doi.org/10.1175/2009JCLI3152.1.

Tukiainen, S., E. O'Connor, and A. Korpinen, 2020: CloudnetPy: A Python package for processing cloud remote sensing data. *J. Open Source Software*, **5**, 2123, https://doi.org/10.21105/joss.02123.

Vignon, E., and Coauthors, 2021: Challenging and improving the simulation of mid-level mixed-phase clouds over the high-latitude southern ocean. *J. Geophys. Res. Atmos.*, **126**, e2020JD033490, https://doi.org/10.1029/2020JD033490.

Walbröl, A., and Coauthors, 2022: Atmospheric temperature, water vapour and liquid water path from two microwave radiometers during MOSAiC. *Sci. Data*, **9**, 534, https://doi.org/10.1038/s41597-022-01504-1.

Weller, R., 2023a: Air chemistry observatory at Neumayer. Accessed 9 September 2023, https://www.awi.de/en/science/long-term-observations/atmosphere/antarctic-neumayer/air-chemistry.html.

——, 2023b: Airchemistry at Neumayer station, Antarctica. 19 datasets, accessed 18 January 2024, https://doi.org/10.1594/PANGAEA.961235.

——, J. Wöltjen, C. Piel, R. Resenberg, D. Wagenbach, G. König-Langlo, and M. Kriews, 2008: Seasonal variability of crustal and marine trace elements in the aerosol at Neumayer station, Antarctica. *Tellus*, **60B**, 742, https://doi.org/10.1111/j.1600-0889.2008.00372.x.

——, A. Minikin, D. Wagenbach, and V. Dreiling, 2011a: Characterization of the inter-annual, seasonal, and diurnal variations of condensation particle concentrations at Neumayer, Antarctica. *Atmos. Chem. Phys.*, **11**, 13243–13257, https://doi.org/10.5194/acp-11-13243-2011.

——, D. Wagenbach, M. Legrand, C. Elsässer, X. Tian-Kunze, and G. König-Langlo, 2011b: Continuous 25-yr aerosol records at coastal Antarctica–I: Inter-annual variability of ionic compounds and links to climate indices. *Tellus*, **63B**, 901, https://doi.org/10.1111/j.1600-0889.2011.00542.x.

Wendisch, M., and Coauthors, 2019: The Arctic cloud puzzle: Using ACLOUD/PASCAL multiplatform observations to unravel the role of clouds and aerosol particles in Arctic amplification. *Bull. Amer. Meteor. Soc.*, **100**, 841–871, https://doi.org/10.1175/BAMS-D-18-0072.1.

Wesche, C., R. Weller, G. König-Langlo, T. Fromm, A. Eckstaller, U. Nixdorf, and E. Kohlberg, 2016: Neumayer III and Kohnen Station in Antarctica operated by the Alfred Wegener Institute. *J. Large-Scale Res. Facil.*, **2**, A85, https://doi.org/10.17815/jlsrf-2-152.

Wex, H., and Coauthors, 2019: Annual variability of ice-nucleating particle concentrations at different Arctic locations. *Atmos. Chem. Phys.*, **19**, 5293–5311, https://doi.org/10.5194/acp-19-5293-2019.

Wille, J. D., and Coauthors, 2024a: The extraordinary March 2022 East Antarctica "heat" wave. Part I: Observations and meteorological drivers. *J. Climate*, **37**, 757–778, https://doi.org/10.1175/JCLI-D-23-0175.1.

——, and Coauthors, 2024b: The extraordinary March 2022 East Antarctica "heat" wave. Part II: Impacts on the Antarctic ice sheet. *J. Climate*, **37**, 779–799, https://doi.org/10.1175/JCLI-D-23-0176.1.

Yin, Z., and H. Baars, 2021: PollyNET/Pollynet_Processing_Chain: Version 3.0. Zenodo, accessed 19 July 2023, https://doi.org/10.5281/ZENODO.5571289.

——, and Coauthors, 2019: Aerosol measurements with a shipborne sun–sky–lunar photometer and collocated multiwavelength Raman polarization lidar over the Atlantic Ocean. *Atmos. Meas. Tech.*, **12**, 5685–5698, https://doi.org/10.5194/amt-12-5685-2019.

Zhang, D., Z. Wang, P. Kollias, A. M. Vogelmann, K. Yang, and T. Luo, 2018: Ice particle production in mid-level stratiform mixed-phase clouds observed with collocated A-Train measurements. *Atmos. Chem. Phys.*, **18**, 4317–4327, https://doi.org/10.5194/acp-18-4317-2018.

——, A. Vogelmann, P. Kollias, E. Luke, F. Yang, D. Lubin, and Z. Wang, 2019: Comparison of Antarctic and Arctic single-layer stratiform mixed-phase cloud properties using ground-based remote sensing measurements. *J. Geophys. Res. Atmos.*, **124**, 10186–10204, https://doi.org/10.1029/2019JD030673.